Expansion of Difference-field Boundary Element Method for Numerical Analyses of Various Local Defects in Periodic Surface Relief Structures

Jun-ichiro Sugisaka,[1,*] Takashi Yasui,[1] and Koichi Hirayama[1]

[1] *Kitami Institute of Technology, Koen-cho 165, Kitami, Hokkaido 090-8507, Japan*

Abstract

We expand the difference-field boundary element method (DFBEM) to calculate wave scattering from a variety of local periodic structure defects. The DFBEM is a numerical method for simulating the diffraction caused by a periodic surface-relief structure with a defect. Although it is more efficient than conventional techniques such as the finite-difference time-domain (FDTD) method, the original DFBEM is limited to projection defects. Here, we derive the integral equations and expressions for crack and buried-pillar defects, and also demonstrate some numerical analyses, validating the results by comparison with results from the FDTD method and the dielectric interface boundary conditions.

OCIS codes: (050.1950) Diffraction gratings; (000.4430) Numerical approximation and analysis; (050.1755) Computational electromagnetic methods.

http://dx.doi.org/10.1364/XX.99.099999

* Corresponding author: sugisaka@mail.kitami-it.ac.jp

1. Introduction

Periodic surface relief structures appear in a variety of optical devices such as diffraction gratings, photonic crystals, plasmonic devices, metamaterials, imaging devices, and photomasks with periodic patterns. For example, diffraction gratings have been applied to chemical analysis, pulsed-light shaping, and optical communication, while photomasks with periodic patterns in lithography systems provide regularly aligned wiring and electrode patterns. In all applications, the periodic surface relief structures must be fabricated with high accuracy. For example, local defects in the periodic structure due to cracks, adherent particles, and fabrication errors generate undesired wave scattering. These scattered waves can affect the diffraction characteristics as well as the system precision and product quality. However, designed defect cavities in photonic crystals, which localize the light waves within the defect, can allow defects to be utilized actively. Thus, finely tuning the defect position, size, and shape is critical for obtaining certain device characteristics such as the quality factor and resonant wavelength.

To improve these optical devices, the influence of defects on the device properties must be analyzed. In general, because the defects are comparable in size to the wavelength, defect analysis requires vectorial electromagnetic field computations to solve Maxwell's equations while considering the boundary conditions at the dielectric interface. Rigorous coupled wave analysis (RCWA), which is also known as the Fourier modal method, the finite difference time domain (FDTD) method, and finite element method (FEM) are popular and versatile numerical methods for performing this analysis. Although RCWA was developed for the analysis of periodic structures, it has also been used to analyze non-periodic structures through the introduction of super-cells [1–3] and absorbing layers [4, 5]. These approaches also allow RCWA to be applied to defective periodic structures. On the other hand, the FDTD method is suitable for both periodic and non-periodic structures. Many devices such as photonic crystals with defects [6], metallic nanoslits [7], photomasks [8, 9], and defective gratings [10] have been analyzed with the FDTD method. The FEM has also been applied to defective photonic crystals [11], defective diffraction gratings [12], and the inverse problem of defective gratings [13].

For the examination of defective structures, a perturbation method is also applied. In this method, the field distribution is divided into unperturbed and scattered fields radiated

from the defects, and the scattered field is solved using tools such as the FEM and the source model technique. To date, defects on perfect conductors have been analyzed using the FEM [14, 15]. Further, problems featuring a single slit in a perfect conductor grating [16] and a local defect in a photonic crystal [17] have been solved using the source model technique.

Other approaches have also been proposed by Sun and Zheng [18] and Watanabe *et al.* [19]. Those methods provide the vectorial-field analysis of defective diffraction gratings.

The boundary element method (BEM) [20, 21] (essentially the same as the method of moments: MoM) is a commonly used numerical method for scattering analyses. In BEM, the fields on the perimeters of the defects, or scatterers, are obtained from integral equations, and the field distributions are then calculated both inside and outside the scatterers using the integral expressions. The integral equations and expressions are obtained from path integrals on the respective boundaries, and the discretization necessary for the integral equations and expressions is limited to the fields on the perimeters of the scatterers. Thus, the BEM can reduce the memory requirements of the calculation and enable efficient computation, whereas the RCWA, FEM, and FDTD methods require a considerable amount of memory because of the discretization of the region in addition to the boundary. Because there is no fictitious light source required in the FDTD method and source model technique, the BEM provides rigorous field distributions that satisfy the Maxwell's equations and dielectric interface boundary conditions everywhere. Periodic surface relief structures such as diffraction gratings are analyzed using only the path integrals in one period through the application of Bloch's theorem [22]. In contrast, similar analyses for non-periodic structures such as defective gratings are very difficult to perform, because the computational cost associated with the discretization on the infinitely long boundary of the grating surface increases considerably. Thus, the BEM and MoM calculations of such optical devices are limited to ridge waveguides when the field is confined in the core [23], finite-sized optical elements [24], narrow illumination areas on optical elements [25], and finite-sized defective etched diffraction gratings [26].

In our previous work, we developed the difference-field boundary element method (DF-BEM) [27] for the analysis of infinitely large defective gratings with plane-wave illumination, which is also based on the perturbation method and the BEM. The field distribution (total field) of a defective grating is divided into two components: a base field and a difference field. The base field is for a non-defect structure, and can be easily calculated using Bloch's

theorem, whereas the difference field is given by solving the integral equations. We eliminated the path integrals on the infinitely-long boundary, so the DFBEM solves the integral equation with path integrals only around the defect, resulting in high-accuracy calculations with a shorter computational time than either the RCWA or FDTD methods. However, the DFBEM is strongly restricted by the topology of the defect structure due to the allowed integration paths in the integral equations. In fact, the original DFBEM described in Ref. [27] can only be applied to gratings with projection defects on the surface, and the feasibility of efficient calculation for other defect types has not yet been investigated.

In this paper, we expand the DFBEM to analyze a variety of defect topologies. First, we present the integral equations and expressions for two additional defect types: crack and buried-pillar defects. Crack defects are formed by removing a part of the groove or substrate, whereas buried-pillar defects are formed by a pillar partially buried in the grating surface. In both cases, the integral equations and expressions are derived in such a way as to remove the infinitely long path integrals. This derivation is discussed in Section 2. In Section 3, the fields obtained by DFBEM are validated using two approaches: (i) the field around the surface of the defective grating is compared with the FDTD method result, and (ii) the fields close to the defect are taken to be verified if they satisfy the electromagnetic boundary conditions on the dielectric interface.

2. Formulation of the integral equations and expressions

First, to simplify the notation of the common terms in the integral equations, we introduce the following integral operators, $\mathcal{I}$ and $\mathcal{I}'$, which are defined as

$$\mathcal{I}^{C}_{p,q}[f] \equiv \int_C \left\{ G_p(\boldsymbol{\rho};\boldsymbol{\rho}') \frac{\partial f(\boldsymbol{\rho}')}{\partial n'} - f(\boldsymbol{\rho}') \frac{\partial G_p(\boldsymbol{\rho};\boldsymbol{\rho}')}{\partial n'} \right\} \mathrm{d}l', \tag{1}$$

$$\mathcal{I}'^{C}_{p,q}[f] \equiv \int_C \left\{ G_p(\boldsymbol{\rho};\boldsymbol{\rho}') \frac{\eta_p}{\eta_q} \frac{\partial f(\boldsymbol{\rho}')}{\partial n'} - f(\boldsymbol{\rho}') \frac{\partial G_p(\boldsymbol{\rho};\boldsymbol{\rho}')}{\partial n'} \right\} \mathrm{d}l'. \tag{2}$$

The integral path, C, is the boundary between the regions, S_p and S_q. Examples of C are shown in Figs. 1(a) and 1(b), which are the cross-sectional schematics of an isolated pillar and semi-infinite scatterer, respectively. The two-dimensional position vector, $\boldsymbol{\rho}$, defines

a position in the cross-sectional plane. The coordinates, (n, l, z), form a local coordinate system on C, where n and l are normal and tangent to C, respectively, and z is perpendicular to n and l. The constant, η_p, is the magnetic permittivity in S_p, in the case of s-polarization, or the electric permittivity in S_p for p-polarization. Finally, G_p is a free-space Green's function for S_p, with

$$G_p(\boldsymbol{\rho}; \boldsymbol{\rho}') = -\frac{j}{4} H_0^{(2)} \left(k_p |\boldsymbol{\rho} - \boldsymbol{\rho}'| \right), \tag{3}$$

where j is an imaginary unit, and $H_0^{(2)}$ is a zeroth-order Hankel function of the second kind. The wavenumber, k_p, is defined by $n_p \omega / c$, where n_p, ω, and c are the refractive index (complex value) in S_p, the angular frequency of the incident field, and the velocity of light in vacuum, respectively. In Eqs. (1) and (2), f is either the z-component of the electric field in the case of s-polarization, or the z-component of the magnetic field in the case of p-polarization. Therefore, the field in S_p is expressed as f_p. The operators, $\mathcal{I}_{p,q}^{C}$ and $\mathcal{I}'^{C}_{p,q}$, operate on the field distribution on C, f.

Both $\mathcal{I}$ and $\mathcal{I}'$ must be used according to the integrand f. When the integrand is f_p (the field on the S_p side of C), the $\mathcal{I}_{p,q}^{C}$ operator must be used, whereas $\mathcal{I}'^{C}_{p,q}$ should be applied for f_q (the field exterior to S_p). In the $\mathcal{I}'^{C}_{p,q}$ operator, the integrand (f_q) and $\partial f_q / \partial n$ are converted to the notation for S_p using the boundary condition on C, such that

$$f_p(\boldsymbol{\rho}) = f_q(\boldsymbol{\rho}), \tag{4}$$

$$\frac{1}{\eta_p} \frac{\partial f_p(\boldsymbol{\rho})}{\partial n} = \frac{1}{\eta_q} \frac{\partial f_q(\boldsymbol{\rho})}{\partial n}. \tag{5}$$

Using these integral operators, the integral equations that describe the field on C [20] can be expressed simply as

$$\frac{1}{2} f_p(\boldsymbol{\rho}) = \mathcal{I}_{p,q}^{C} \left[f_p \right], \quad (\boldsymbol{\rho} \in C), \tag{6}$$

$$\frac{1}{2} f_p(\boldsymbol{\rho}) = f_q^{\mathrm{inc}}(\boldsymbol{\rho}) - \mathcal{I}'^{C}_{q,p} \left[f_p \right], \quad (\boldsymbol{\rho} \in C), \tag{7}$$

where f^{inc} is the incident field and f_p is an unknown variable. Since f_p in Eq. (7) is the field exterior to the S_q side, we must use $\mathcal{I}'_{q,p}$ instead of $\mathcal{I}_{q,p}$.

After solving Eqs. (6) and (7), the $f_p(\boldsymbol{\rho})$ and $f_q(\boldsymbol{\rho})$ fields, excluding $\boldsymbol{\rho} \in C$, are given by the following integral expressions

$$f_p(\boldsymbol{\rho}) = \mathcal{I}_{p,q}^{C} \left[f_p \right], \quad (\boldsymbol{\rho} \in \mathrm{S}_p), \tag{8}$$

$$f_q(\boldsymbol{\rho}) = f_q^{\mathrm{inc}}(\boldsymbol{\rho}) - \mathcal{I}'^{C}_{q,p} \left[f_p \right] m \quad (\boldsymbol{\rho} \in \mathrm{S}_q). \tag{9}$$

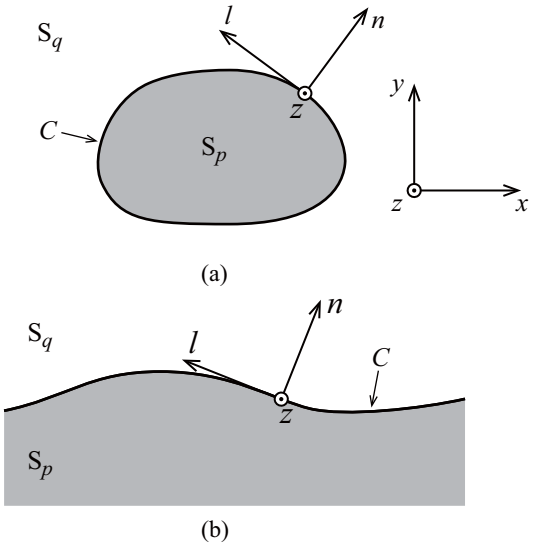

Fig. 1. Cross-sectional schematic of (a) an isolated scatterer and (b) a semi-infinite scatterer in free space, where S_p and S_q are the interior and exterior regions of the scatterer, respectively, and C is the boundary between them.

2.A. Pattern I: Projection defect

We first describe the integral equation for a projection defect [27], in order to compare it with the crack and buried-pillar defects discussed below. Projection defects occur when part of the substrate material extends outside the grating or adheres to the dielectrics on the groove surface. The cross-sectional schematic is shown in Fig. 2(a). Here S_1, S_2, and S_3 are the interior grating (within the grating), exterior grating (outside the grating), and interior defect (within the defect) regions, respectively. Each region must be composed of the same uniform material. If the refractive index, n_3, in S_3 is equal to the refractive index, n_1, in S_1 ($n_3 = n_1$), then S_3 represents a projection. Otherwise, if $n_3 \neq n_1$, S_3 represents an adherent dielectric. The integral equations consist of path integrals on the C_0, C_1, and C_2 boundaries, where C_0 (solid line in Fig. 2) is the surface of the substrate excluding the defect, C_1 (dotted line in Fig. 2) is the boundary between the defect and the grating, and C_2 (dashed line in Fig. 2) is the boundary on the defect surface.

First, we represent the total field distributions in S_1, S_2, and S_3 as $f_1 + \Delta f_1$, $f_2 + \Delta f_2$, and f_3, respectively. For S_1 and S_2, the total fields are expressed by the sum of the base field, f_1 or f_2, and the difference field is Δf_1 or Δf_2. We obtain the integral equations such

that

$$\frac{1}{2}f_1(\boldsymbol{\rho}) + \frac{1}{2}\Delta f_1(\boldsymbol{\rho}) = \mathcal{I}_{1,2}^{C_0}\left[f_1 + \Delta f_1\right] + \mathcal{I}'^{C_1}_{1,3}\left[f_3\right], \quad (\boldsymbol{\rho} \in C_0), \tag{10}$$

$$\frac{1}{2}f_3(\boldsymbol{\rho}) = \mathcal{I}_{1,2}^{C_0}\left[f_1 + \Delta f_1\right] + \mathcal{I}'^{C_1}_{1,3}\left[f_3\right], \quad (\boldsymbol{\rho} \in C_1), \tag{11}$$

$$\frac{1}{2}f_2(\boldsymbol{\rho}) + \frac{1}{2}\Delta f_2(\boldsymbol{\rho}) = f^{\mathrm{inc}}(\boldsymbol{\rho}) - \mathcal{I}'^{C_0}_{2,1}\left[f_1 + \Delta f_1\right] - \mathcal{I}'^{C_2}_{2,3}\left[f_3\right], \quad (\boldsymbol{\rho} \in C_0), \tag{12}$$

$$\frac{1}{2}f_3(\boldsymbol{\rho}) = f^{\mathrm{inc}}(\boldsymbol{\rho}) - \mathcal{I}'^{C_0}_{2,1}\left[f_1 + \Delta f_1\right] - \mathcal{I}'^{C_2}_{2,3}\left[f_3\right], \quad (\boldsymbol{\rho} \in C_2), \tag{13}$$

$$\frac{1}{2}f_3(\boldsymbol{\rho}) = -\mathcal{I}_{3,1}^{C_1}\left[f_3\right] + \mathcal{I}_{3,2}^{C_2}\left[f_3\right], \quad (\boldsymbol{\rho} \in C_1), \tag{14}$$

$$\frac{1}{2}f_3(\boldsymbol{\rho}) = -\mathcal{I}_{3,1}^{C_1}\left[f_3\right] + \mathcal{I}_{3,2}^{C_2}\left[f_3\right], \quad (\boldsymbol{\rho} \in C_2). \tag{15}$$

However, this set of equations is unsuitable for numerical calculation because Eqs. (10)–(13) contain path integrals on C_0, which is an infinitely long boundary. Next, we consider the non-defective grating shown in Fig. 2(b). The boundary of the structure consists of C_0 and C_1 and, thus, the following equations are composed of path integrals on C_0 and C_1, such that

$$\frac{1}{2}f_1(\boldsymbol{\rho}) = \mathcal{I}_{1,2}^{C_0}\left[f_1\right] + \mathcal{I}_{1,2}^{C_1}\left[f_1\right], \quad (\boldsymbol{\rho} \in C_0), \tag{16}$$

$$\frac{1}{2}f_1(\boldsymbol{\rho}) = \mathcal{I}_{1,2}^{C_0}\left[f_1\right] + \mathcal{I}_{1,2}^{C_1}\left[f_1\right], \quad (\boldsymbol{\rho} \in C_1), \tag{17}$$

$$\frac{1}{2}f_2(\boldsymbol{\rho}) = f^{\mathrm{inc}}(\boldsymbol{\rho}) - \mathcal{I}'^{C_0}_{2,1}\left[f_1\right] - \mathcal{I}'^{C_1}_{2,1}\left[f_1\right], \quad (\boldsymbol{\rho} \in C_0), \tag{18}$$

$$f_2(\boldsymbol{\rho}) = f^{\mathrm{inc}}(\boldsymbol{\rho}) - \mathcal{I}'^{C_0}_{2,1}\left[f_1\right] - \mathcal{I}'^{C_1}_{2,1}\left[f_1\right], \quad (\boldsymbol{\rho} \in C_2). \tag{19}$$

By performing the following subtractions: Eq. (10)−Eq. (16), Eq. (11)−Eq. (17), Eq.

(12)−Eq. (18), and Eq. (13)−Eq. (19), we find

$$\begin{aligned}
\frac{1}{2}\Delta f_1(\boldsymbol{\rho}) =& \mathcal{I}_{1,2}^{C_0}\left[\Delta f_1\right] + \mathcal{I}'^{C_1}_{1,3}\left[f_3\right] \\
&- \mathcal{I}_{1,2}^{C_1}\left[f_1\right], \quad (\boldsymbol{\rho} \in C_0), \qquad (20)\\
\frac{1}{2}f_3(\boldsymbol{\rho}) - \frac{1}{2}f_1(\boldsymbol{\rho}) =& \mathcal{I}_{1,2}^{C_0}\left[\Delta f_1\right] + \mathcal{I}'^{C_1}_{1,3}\left[f_3\right] \\
&- \mathcal{I}_{1,2}^{C_1}\left[f_1\right], \quad (\boldsymbol{\rho} \in C_1), \qquad (21)\\
\frac{1}{2}\Delta f_1(\boldsymbol{\rho}) =& -\mathcal{I}'^{C_0}_{2,1}\left[\Delta f_1\right] - \mathcal{I}'^{C_2}_{2,3}\left[f_3\right] \\
&+ \mathcal{I}'^{C_1}_{2,1}\left[f_1\right], \quad (\boldsymbol{\rho} \in C_0), \qquad (22)\\
\frac{1}{2}f_3(\boldsymbol{\rho}) - f_2(\boldsymbol{\rho}) =& -\mathcal{I}'^{C_0}_{2,1}\left[\Delta f_1\right] - \mathcal{I}'^{C_2}_{2,3}\left[f_3\right] \\
&+ \mathcal{I}'^{C_1}_{2,1}\left[f_1\right], \quad (\boldsymbol{\rho} \in C_2). \qquad (23)
\end{aligned}$$

To obtain the left-hand side of Eqs. (22), we replace f_2 and Δf_2 by f_1 and Δf_1, respectively, by applying the boundary conditions $f_1 = f_2$ and $f_1 + \Delta f_1 = f_2 + \Delta f_2$ on C_0. We assume that the integrand, Δf_1, for the integral on C_0 decays to zero with increasing distance from the defect. Under this assumption, it is possible to truncate C_0 around the defect without affecting the accuracy of the solution. This assumption is valid as long as any propagation mode that propagates along the grating surface does not exist, because Δf_1 is an outgoing wave radiated from the scatterer S_3, reducing its amplitude with propagation distance (the wavefronts are shown in Section 3). Any propagation mode does not exist when S_1 and S_2 consist of non-conductive dielectrics. In contrast, when S_1 consists of a metal and the incident wave is $p-$polarization, the radiated wave excites the surface plasmon polariton modes on C_0. Those modes keep the amplitude constant along the surface, and do not decay with increasing distance from the defect.

Eqs. (14), (15), and (20)–(23) form a set of simultaneous equations, with Δf_1 on C_0 and f_3 on C_1 and C_2 as unknown variables. The $\mathcal{I}_{1,2}^{C_1}\left[f_1\right]$ terms in Eqs. (20) and (21), $f_1(\boldsymbol{\rho})/2$ in Eq. (21), and $f_1(\boldsymbol{\rho})$ in Eq. (23) are constant terms given by f_1 on C_1 and C_2 and $\partial f_1/\partial n$ on C_1. In other words, it is possible to solve the integral equation using the base field along the defect outline.

The calculation cost (the operation number) required for the solution of the simultaneous equations is $O(N^3)$, when direct solvers such as Gauss's elimination method and LU decomposition are applied. Here, N is the number of unknown variables, which depends on

the truncated length of C_0 and the length of the defect perimeter (C_1 and C_2). When N is extremely large, that fast multipole method (FMM) [28, 29] with an iterative solver is applicable, as well as the conventional BEM. In that case, the number of necessary resources is $O(N)$, for large N [30].

Similar to the previous step, the integral expressions can be obtained by subtracting the integral expressions for defective and non-defective structures, such that

$$\Delta f_1(\boldsymbol{\rho}) = \mathcal{I}_{1,2}^{C_0}[\Delta f_1] + \mathcal{I}'^{C_1}_{1,3}[f_3] - \mathcal{I}_{1,2}^{C_1}[f_1], \quad (\boldsymbol{\rho} \in \mathrm{S}_1), \tag{24}$$

$$\Delta f_2(\boldsymbol{\rho}) = -\mathcal{I}'^{C_0}_{2,1}[\Delta f_1] - \mathcal{I}'^{C_2}_{2,3}[f_3] + \mathcal{I}'^{C_1}_{2,1}[f_1], \quad (\boldsymbol{\rho} \in \mathrm{S}_2), \tag{25}$$

$$f_3(\boldsymbol{\rho}) = -\mathcal{I}_{3,1}^{C_1}[f_3] + \mathcal{I}_{3,2}^{C_2}[f_3], \quad (\boldsymbol{\rho} \in \mathrm{S}_3). \tag{26}$$

The difference field distribution is given by calculating these integral expressions ($O(N)$ operation) for different $\boldsymbol{\rho}$. Thus, the total number of resources required to obtain the difference field distribution is $O(MN)$, where M is the number of discretized points in the field distribution.

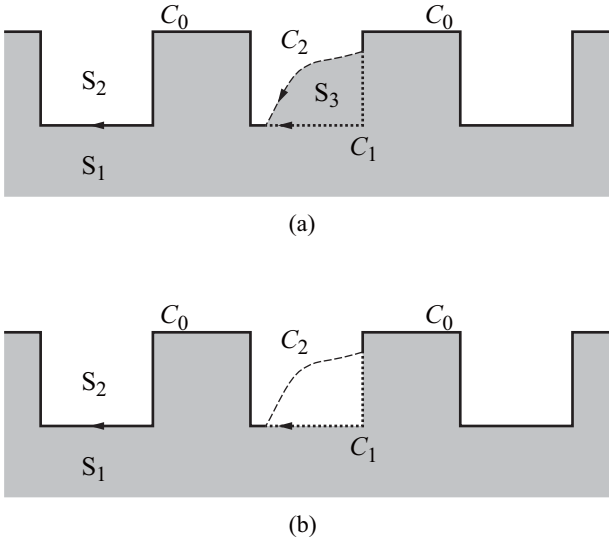

Fig. 2. Cross-sectional schematic of a grating (a) with a projection defect and (b) without a defect, where S_1, S_2, and S_3 are the interior grating, exterior grating, and interior defect regions, respectively. The boundaries on the grating (solid lines), between the defect and the grating (dotted lines), and on the surface of the defect (dashed lines) are denoted by C_0, C_1, and C_2, respectively. The arrows on C_0, C_1, and C_2 denote the path integral directions (direction of the l coordinate).

2.B. Pattern II: Crack defect

A crack defect occurs when part of the substrate material vanishes because of mechanical cracks or fabrication errors, or when the refractive index of a groove surface is locally altered as a result of factors such as oxidation. The cross-sectional schematic is shown in Fig. 3(a). The S_1, S_2, and S_3 terms have the same meaning as in the previous section. Here, if n_3 is set such that $n_3 = n_2$, then S_3 represents a crack. Otherwise, S_3 represents an altered dielectric. The integral equations consist of path integrals on the C_0, C_1, and C_2 boundaries, as shown in Fig. 3(a), where C_0 (solid line in Fig. 3) is the surface of the substrate excluding the defect, C_1 (dotted line in Fig. 3) is the boundary between S_2 and S_3, and C_2 (dashed line in Fig. 3) is the crack surface.

First, we consider the defective grating. Similar to Pattern I, we denote the total fields in S_1, S_2, and S_3 as $f_1 + \Delta f_1$, $f_2 + \Delta f_2$, and f_3, respectively. Because the perimeter of S_1 is defined by C_0 and C_2, the integral equation, Eq. (6), at any $\boldsymbol{\rho} \in C_0$ and C_2, satisfies

$$\begin{aligned}\frac{1}{2}f_1(\boldsymbol{\rho}) + \frac{1}{2}\Delta f_1(\boldsymbol{\rho}) =& \mathcal{I}_{1,2}^{C_0}\left[f_1 + \Delta f_1\right] \\ &+ \mathcal{I}'^{C_2}_{1,3}\left[f_3\right], \quad (\boldsymbol{\rho} \in C_0),\end{aligned} \tag{27}$$

$$\frac{1}{2}f_3(\boldsymbol{\rho}) = \mathcal{I}_{1,2}^{C_0}\left[f_1 + \Delta f_1\right] + \mathcal{I}'^{C_2}_{1,3}\left[f_3\right], \quad (\boldsymbol{\rho} \in C_2). \tag{28}$$

In Eqs. (27) and (28), we have expressed the total field on C_2 by f_3 instead of $f_1(\boldsymbol{\rho}) + \Delta f_1(\boldsymbol{\rho})$. Because f_3 does not denote the field on the S_1 side, the operator associated with f_3 must be $\mathcal{I}'^{C_2}_{1,3}$ instead of $\mathcal{I}^{C_2}_{1,3}$. Similar to the integral equation, Eq. (7), the path integral along C_0 and C_1, which surrounds the S_2 region, must satisfy the following equations:

$$\begin{aligned}\frac{1}{2}f_2(\boldsymbol{\rho}) + \frac{1}{2}\Delta f_2(\boldsymbol{\rho}) =& f^{\mathrm{inc}}(\boldsymbol{\rho}) - \mathcal{I}'^{C_0}_{2,1}\left[f_1 + \Delta f_1\right] \\ &- \mathcal{I}'^{C_1}_{2,3}\left[f_3\right], \quad (\boldsymbol{\rho} \in C_0),\end{aligned} \tag{29}$$

$$\begin{aligned}\frac{1}{2}f_3(\boldsymbol{\rho}) =& f^{\mathrm{inc}}(\boldsymbol{\rho}) - \mathcal{I}'^{C_0}_{2,1}\left[f_1 + \Delta f_1\right] \\ &- \mathcal{I}'^{C_1}_{2,3}\left[f_3\right], \quad (\boldsymbol{\rho} \in C_1).\end{aligned} \tag{30}$$

Because the integrands of $\mathcal{I}'^{C_0}_{2,1}\left[f_1 + \Delta f_1\right]$ and $\mathcal{I}'^{C_1}_{2,3}\left[f_3\right]$ describe the exterior of S_2, we must use $\mathcal{I}'$ instead of $\mathcal{I}$. For the S_3 region, the integral equations are given by the path integral

along the perimeter boundaries, C_1 and C_2, as

$$\frac{1}{2}f_3(\boldsymbol{\rho}) = \mathcal{I}_{3,2}^{C_1}[f_3] - \mathcal{I}_{3,1}^{C_2}[f_3], \quad (\boldsymbol{\rho} \in C_1), \tag{31}$$

$$\frac{1}{2}f_3(\boldsymbol{\rho}) = \mathcal{I}_{3,2}^{C_1}[f_3] - \mathcal{I}_{3,1}^{C_2}[f_3], \quad (\boldsymbol{\rho} \in C_2). \tag{32}$$

Next, we consider the non-defective grating shown in Fig. 3(b). The field distributions inside S_1 and S_2 are expressed as f_1 and f_2, respectively. Because C_0 is a part of the boundary that surrounds S_1, any $\boldsymbol{\rho} \in C_0$ satisfies

$$\frac{1}{2}f_1(\boldsymbol{\rho}) = \mathcal{I}_{1,2}^{C_0}[f_1] + \mathcal{I}_{1,2}^{C_1}[f_1], \quad (\boldsymbol{\rho} \in C_0). \tag{33}$$

Moreover, $\boldsymbol{\rho} \in C_2$ is a point in S_1; therefore, $f_1(\boldsymbol{\rho})$ is given by the path integrals along C_0 and C_1 surrounding S_1, such that

$$f_1(\boldsymbol{\rho}) = \mathcal{I}_{1,2}^{C_0}[f_1] + \mathcal{I}_{1,2}^{C_1}[f_1], \quad (\boldsymbol{\rho} \in C_2). \tag{34}$$

For the S_2 region, any point $\boldsymbol{\rho} \in C_0$ and C_1 satisfies

$$\frac{1}{2}f_2(\boldsymbol{\rho}) = f^{\mathrm{inc}}(\boldsymbol{\rho}) - \mathcal{I}'^{C_0}_{2,1}[f_1] - \mathcal{I}'^{C_1}_{2,1}[f_1], \quad (\boldsymbol{\rho} \in C_0), \tag{35}$$

$$\frac{1}{2}f_2(\boldsymbol{\rho}) = f^{\mathrm{inc}}(\boldsymbol{\rho}) - \mathcal{I}'^{C_0}_{2,1}[f_1] - \mathcal{I}'^{C_1}_{2,1}[f_1], \quad (\boldsymbol{\rho} \in C_1). \tag{36}$$

Note that the integrands on the right-hand side in Eqs. (35) and (36) are the exterior field of S_2; thus, we must use $\mathcal{I}'$ instead of $\mathcal{I}$.

By performing the following subtractions: Eq. (27)−Eq. (33), Eq. (28)−Eq. (34), Eq. (29)−Eq. (35), and Eq. (30)−Eq. (36), we find

$$\begin{aligned}\frac{1}{2}\Delta f_1(\boldsymbol{\rho}) =& \mathcal{I}_{1,2}^{C_0}[\Delta f_1] + \mathcal{I}'^{C_2}_{1,3}[f_3] \\ &- \mathcal{I}_{1,2}^{C_1}[f_1], \quad (\boldsymbol{\rho} \in C_0),\end{aligned} \tag{37}$$

$$\begin{aligned}\frac{1}{2}f_3(\boldsymbol{\rho}) - f_1(\boldsymbol{\rho}) =& \mathcal{I}_{1,2}^{C_0}[\Delta f_1] + \mathcal{I}'^{C_2}_{1,3}[f_3] \\ &- \mathcal{I}_{1,2}^{C_1}[f_1], \quad (\boldsymbol{\rho} \in C_2),\end{aligned} \tag{38}$$

$$\begin{aligned}\frac{1}{2}\Delta f_1(\boldsymbol{\rho}) =& -\mathcal{I}'^{C_0}_{2,1}[\Delta f_1] - \mathcal{I}'^{C_1}_{2,3}[f_3] \\ &+ \mathcal{I}'^{C_1}_{2,1}[f_1], \quad (\boldsymbol{\rho} \in C_0),\end{aligned} \tag{39}$$

$$\begin{aligned}\frac{1}{2}f_3(\boldsymbol{\rho}) - \frac{1}{2}f_1(\boldsymbol{\rho}) =& -\mathcal{I}'^{C_0}_{2,1}[\Delta f_1] - \mathcal{I}'^{C_1}_{2,3}[f_3] \\ &+ \mathcal{I}'^{C_1}_{2,1}[f_1], \quad (\boldsymbol{\rho} \in C_1).\end{aligned} \tag{40}$$

To obtain Eqs. (39) and (40), we replaced f_2 and Δf_2 on the left-hand sides by f_1 and Δf_1, respectively, by applying the boundary condition on C_0 ($f_1 = f_2$ and $f_1 + \Delta f_1 = f_2 + \Delta f_2$) and that on C_1 ($f_1 = f_2$).

Eqs. (31), (32), and (37)–(40) form a set of simultaneous equations. As well as the projection defects (Pattern I), we assume that the integrand, Δf_1, of the path integrals on C_0 decays to zero with increasing distance from the defect. Therefore, similar to the procedure in Pattern I, we can truncate C_0 around the defects without affecting the solution. The simultaneous equation provides the solutions for Δf_1 and $\partial \Delta f_1/\partial n$ on C_0 as well as f_3 and $\partial \Delta f_3/\partial n$ on C_1 and C_2. The constant terms are given by the base field on the perimeter of the defect: f_1 on C_2 as well as f_1 and $\partial \Delta f_1/\partial n$ on C_1. If the size of the defect and the truncated length of C_0 are equal to those for Pattern I, the computational cost of Pattern II is the same as that of Pattern I. The FMM is also applicable for solving the simultaneous equation.

As previously, the integral expressions are given by subtracting the integral expressions for the defective and non-defective structures, such that

$$\Delta f_1(\boldsymbol{\rho}) = \mathcal{I}_{1,2}^{C_0}[\Delta f_1] + \mathcal{I}'^{C_2}_{1,3}[f_3] - \mathcal{I}_{1,2}^{C_1}[f_1], \quad (\boldsymbol{\rho} \in \mathrm{S}_1), \tag{41}$$

$$\Delta f_2(\boldsymbol{\rho}) = -\mathcal{I}'^{C_0}_{2,1}[\Delta f_1] - \mathcal{I}'^{C_1}_{2,3}[f_3] + \mathcal{I}'^{C_1}_{2,1}[f_1], \quad (\boldsymbol{\rho} \in \mathrm{S}_2), \tag{42}$$

$$f_3(\boldsymbol{\rho}) = \mathcal{I}_{3,2}^{C_1}[f_3] - \mathcal{I}_{3,1}^{C_2}[f_3], \quad (\boldsymbol{\rho} \in \mathrm{S}_3). \tag{43}$$

The integrands on the right-hand sides are the base field and the solution of the simultaneous equation. Thus, Eqs. (41)–(43) are solvable after the simultaneous equations have been solved.

2.C. Pattern III: Buried-pillar defect

A buried-pillar defect occurs when a pillar becomes partially embedded in the grating. The cross-sectional schematic of the defective grating is shown in Fig. 4(a). The S_3 region is the cross-section of the pillar, C_0 is the substrate surface excluding the defect, and C_1 is the boundary that disappears when the defect is introduced. Finally, C_2 and C_3 are the perimeters of the defect on the S_2 and S_1 sides, respectively.

First, we represent the total field distributions in S_1, S_2, and S_3 as $f_1 + \Delta f_1$, $f_2 + \Delta f_2$, and f_3, respectively. The boundary of the S_1 region is defined by C_0 and C_3 and, thus, we

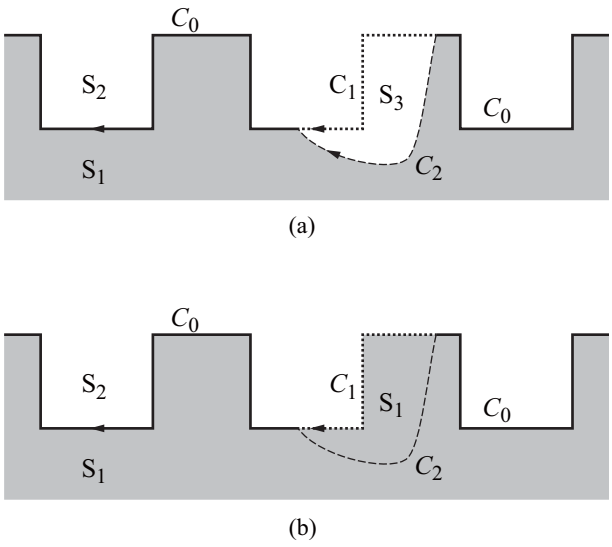

Fig. 3. Cross-sectional schematic of a grating (a) with a crack defect and (b) without a defect, where S_1, S_2, and S_3 have the same meanings as in the previous figure. The boundaries on the grating (solid lines), that which disappears by the crack (dotted lines), and on the surface of the crack (dashed lines) are labeled as C_0, C_1, and C_2, respectively. The arrows on C_0, C_1, and C_2 denote the path integral directions (direction of the l coordinate).

write

$$\begin{aligned}\frac{1}{2}f_1(\boldsymbol{\rho})+\frac{1}{2}\Delta f_1(\boldsymbol{\rho}) =&\mathcal{I}_{1,2}^{C_0}\left[f_1+\Delta f_1\right]\\ &+\mathcal{I}'^{C_3}_{1,3}\left[f_3\right], \quad (\boldsymbol{\rho}\in C_0), \qquad (44)\\ \frac{1}{2}f_3(\boldsymbol{\rho}) =&\mathcal{I}_{1,2}^{C_0}\left[f_1+\Delta f_1\right]\\ &+\mathcal{I}'^{C_3}_{1,3}\left[f_3\right], \quad (\boldsymbol{\rho}\in C_3). \qquad (45)\end{aligned}$$

The operators in the second terms of the right-hand side in Eqs. (44) and (45) are $\mathcal{I}'$ because these integrands (f_3) are exterior to S_1. The integral equations for S_2 are given by the path integral along C_0 and C_2, such that

$$\begin{aligned}\frac{1}{2}f_2(\boldsymbol{\rho})+\frac{1}{2}\Delta f_2(\boldsymbol{\rho}) =&f^{\mathrm{inc}}(\boldsymbol{\rho})-\mathcal{I}'^{C_0}_{2,1}\left[f_1+\Delta f_1\right]\\ &-\mathcal{I}'^{C_2}_{2,3}\left[f_3\right], \quad (\boldsymbol{\rho}\in C_0), \qquad (46)\\ \frac{1}{2}f_3(\boldsymbol{\rho}) =&f^{\mathrm{inc}}(\boldsymbol{\rho})-\mathcal{I}'^{C_0}_{2,1}\left[f_1+\Delta f_1\right]\\ &-\mathcal{I}'^{C_2}_{2,3}\left[f_3\right], \quad (\boldsymbol{\rho}\in C_2). \qquad (47)\end{aligned}$$

The original term on the left-hand side of Eq. (47), $f_2(\boldsymbol{\rho})/2 + \Delta f_2(\boldsymbol{\rho})/2$, has been replaced with $f_3(\boldsymbol{\rho})/2$. For the S_3 region, the following equations are satisfied:

$$\frac{1}{2}f_3(\boldsymbol{\rho}) = \mathcal{I}_{3,2}^{C_2}[f_3] - \mathcal{I}_{3,1}^{C_3}[f_3], \quad (\boldsymbol{\rho} \in C_2), \tag{48}$$

$$\frac{1}{2}f_3(\boldsymbol{\rho}) = \mathcal{I}_{3,2}^{C_2}[f_3] - \mathcal{I}_{3,1}^{C_3}[f_3], \quad (\boldsymbol{\rho} \in C_3). \tag{49}$$

Next, we consider the non-defective grating case, as shown in Fig. 4(b). The following equations are satisfied for the S_1 region, where

$$\frac{1}{2}f_1(\boldsymbol{\rho}) = \mathcal{I}_{1,2}^{C_0}[f_1] + \mathcal{I}_{1,2}^{C_1}[f_1], \quad (\boldsymbol{\rho} \in C_0), \tag{50}$$

$$f_1(\boldsymbol{\rho}) = \mathcal{I}_{1,2}^{C_0}[f_1] + \mathcal{I}_{1,2}^{C_1}[f_1], \quad (\boldsymbol{\rho} \in C_3). \tag{51}$$

Likewise, the following equations are satisfied for S_2:

$$\frac{1}{2}f_2(\boldsymbol{\rho}) = f^{\mathrm{inc}}(\boldsymbol{\rho}) - \mathcal{I}'^{C_0}_{2,1}[f_1] - \mathcal{I}'^{C_1}_{2,1}[f_1], \quad (\boldsymbol{\rho} \in C_0), \tag{52}$$

$$f_2(\boldsymbol{\rho}) = f^{\mathrm{inc}}(\boldsymbol{\rho}) - \mathcal{I}'^{C_0}_{2,1}[f_1] - \mathcal{I}'^{C_1}_{2,1}[f_1], \quad (\boldsymbol{\rho} \in C_2). \tag{53}$$

By performing the following subtractions: Eq. (44)−Eq. (50), Eq. (45)−Eq. (51), Eq. (46)−Eq. (52), and Eq. (47)−Eq. (53), we find

$$\begin{aligned}\frac{1}{2}\Delta f_1(\boldsymbol{\rho}) =& \mathcal{I}_{1,2}^{C_0}[\Delta f_1] + \mathcal{I}'^{C_3}_{1,3}[f_3] \\ & - \mathcal{I}_{1,2}^{C_1}[f_1], \quad (\boldsymbol{\rho} \in C_0),\end{aligned} \tag{54}$$

$$\begin{aligned}\frac{1}{2}f_3(\boldsymbol{\rho}) - f_1(\boldsymbol{\rho}) =& \mathcal{I}_{1,2}^{C_0}[\Delta f_1] + \mathcal{I}'^{C_3}_{1,3}[f_3] \\ & - \mathcal{I}_{1,2}^{C_1}[f_1], \quad (\boldsymbol{\rho} \in C_3),\end{aligned} \tag{55}$$

$$\begin{aligned}\frac{1}{2}\Delta f_1(\boldsymbol{\rho}) =& -\mathcal{I}'^{C_0}_{2,1}[\Delta f_1] - \mathcal{I}'^{C_2}_{2,3}[f_3] \\ & + \mathcal{I}'^{C_1}_{2,1}[f_1], \quad (\boldsymbol{\rho} \in C_0),\end{aligned} \tag{56}$$

$$\begin{aligned}\frac{1}{2}f_3(\boldsymbol{\rho}) - f_2(\boldsymbol{\rho}) =& -\mathcal{I}'^{C_0}_{2,1}[\Delta f_1] - \mathcal{I}'^{C_2}_{2,3}[f_3] \\ & + \mathcal{I}'^{C_1}_{2,1}[f_1], \quad (\boldsymbol{\rho} \in C_2).\end{aligned} \tag{57}$$

To obtain Eq. (56), we replaced f_2 on the left-hand side with f_1 by applying the boundary condition on C_0 ($f_1 = f_2$ and $f_1 + \Delta f_1 = f_2 + \Delta f_2$).

Eqs. (48), (49), and (54)–(57) form a set of simultaneous equations. The integrand for the path integral on C_0 remains only for Δf_1. Similar to the integral equations for Patterns

I and II, we assume that the Δf_1 on C_0 decays to zero with increasing distance from the defect. Therefore, it is possible to truncate the path (C_0) around the defect without affecting the solution. The unknown variables are Δf_1 and $\partial \Delta f_1/\partial n$ on C_0 as well as f_3 and $\partial f_3/\partial n$ on both C_2 and C_3. The constant terms require the base field: f_1 and $\partial f_1/\partial n$ on C_1, f_2 on C_2, and f_1 on C_3. Since any unknown variable is not assigned on C_1, which passes across the defect, the number of unknown variables is determined by the truncated length of C_0 and the length of the defect perimeter (C_2 and C_3). Therefore, the computational cost is comparable to that of Pattern I. The FMM is also applicable to solving the simultaneous equations.

As previously, the integral expressions for S_1, S_2, and S_3 are given by the subtraction of the integral expressions for defective and non-defective structures, such that

$$\Delta f_1(\boldsymbol{\rho}) = \mathcal{I}_{1,2}^{C_0}[\Delta f_1] + \mathcal{I}'^{C_3}_{1,3}[f_3] - \mathcal{I}_{1,2}^{C_1}[f_1], \quad (\boldsymbol{\rho} \in \mathrm{S}_1), \tag{58}$$

$$\Delta f_2(\boldsymbol{\rho}) = -\mathcal{I}'^{C_0}_{2,1}[\Delta f_1] - \mathcal{I}'^{C_2}_{2,3}[f_3] + \mathcal{I}'^{C_1}_{2,1}[f_1], \quad (\boldsymbol{\rho} \in \mathrm{S}_2), \tag{59}$$

$$f_3(\boldsymbol{\rho}) = \mathcal{I}_{3,2}^{C_2}[f_3] - \mathcal{I}_{3,1}^{C_3}[f_3], \quad (\boldsymbol{\rho} \in \mathrm{S}_3). \tag{60}$$

3. Validity of DFBEM

To verify the integral equations and expressions derived in the previous section, we performed calculations on defective gratings corresponding to Patterns I, II, and III. The calculation results were verified in two ways: the field distribution around the defect should agree with that given by the FDTD technique, and the field on the defect perimeter should satisfy the boundary conditions expressed in Eqs. (4) and (5).

For the three defective gratings, the groove period, T, the groove width, and the groove depth were set to 3.5λ ($\lambda \equiv 2\pi c/\omega$), $0.5T$, and $0.3T$, respectively. The cross sections before adding the defects are sketched in Fig. 5. The refractive indices for the interior and exterior of the gratings were 1.5 and 1.0, respectively. The incident field was p-polarized, and the amplitude of the magnetic field was 1.0. The field distributions for p-polarization have sharp (non-differentiable) profiles at the dielectric boundaries according to Eq. (5), whereas the s-polarized field always yields smooth profiles. Hence, in p-polarization, we can easily find boundary condition errors in the calculated field profiles. The propagation direction was

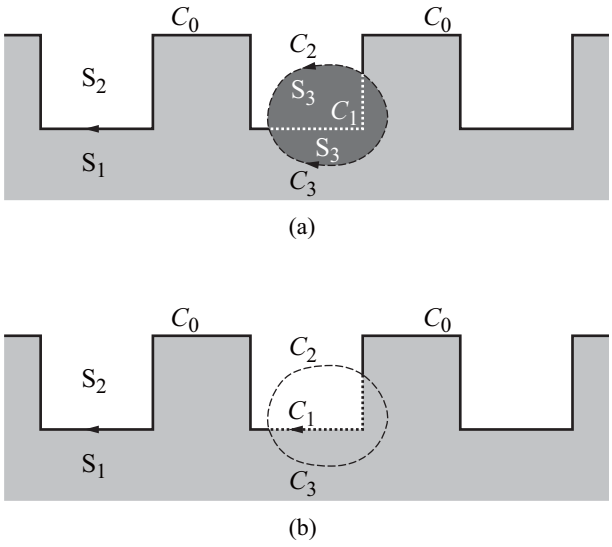

Fig. 4. Cross-sectional schematic of a grating (a) with a buried-pillar defect and (b) without a defect, where S_1, S_2, and S_3 have the same meanings as previously. The boundaries on the grating (solid lines) and that which disappears when the defect is introduced (dotted lines) are denoted by C_0 and C_1, respectively. The pillar surfaces between S_2 and S_3 and between S_1 and S_3 are denoted by C_2 and C_3, respectively. The arrows on C_0, C_1, C_2, and C_3 denote the path integral directions (direction of the l coordinate).

set to $-45°$, which is the angle between the x axis (parallel to the grating surface) and the incident wave vector. The base fields, f_1 and f_2, were calculated using the BEM [22], while the numerical calculation of the base fields and difference fields was performed by discretizing the boundaries with line segments (boundary elements). The lengths of the boundary elements were set to approximately $\lambda/12$, and the field and its n-derivative were considered to be constant within a given boundary element (constant boundary element). We solved the integral (simultaneous) equations using LU decomposition in the LAPACK library. In the difference field calculations, the infinite boundary (C_0) was truncated at $x = \pm 5.25T$ (the origin, $x = 0$ is indicated in Fig. 5). Defects for Patterns I, II, and III are aligned near $x = 0$. The rectangular area around the defect was discretized by 841×266 points with an interval of $\lambda/40$, and we obtained the difference field for each point with integral expressions.

In the FDTD calculation, the analysis area in $-15T \leq x \leq 15T$ was discretized by square Yee's cells with $\lambda/40$ on each side. The incident plane wave was excited by a line

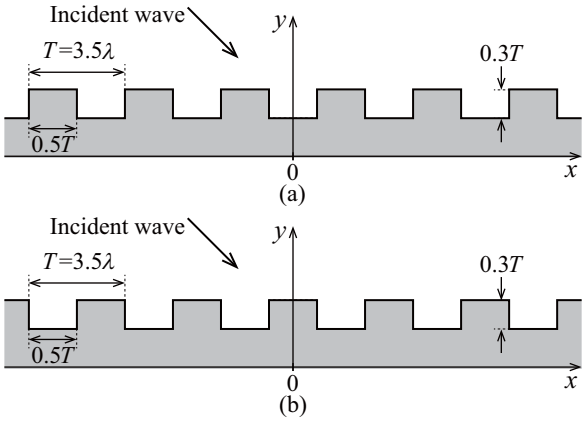

Fig. 5. Cross sections of the periodic gratings before adding defects. The groove period T is 3.5λ. The groove width and height are $0.5T$ and $0.3T$. The refractive indices for the interior and exterior of the gratings are 1.5 and 1.0, respectively. The incident wave is a plane wave of p-polarization.

source, which was placed external to the grating, parallel to the x axis. We placed Bloch's boundary conditions on the perimeters of the analysis area, $x = \pm 15T$, and also positioned perfectly matched absorbing layers on the other edges. Bloch's boundary condition enables the propagation of the incident plane wave in the analysis area without deformation near the boundaries at $x = \pm 15T$. For comparison with the DFBEM, the obtained field distributions were trimmed so as to be the same size as those of the DFBEM.

For a comparison of computational costs, each computation was performed with the same computer (a workstation with an Intel Xeon CPU 3.20 GHz and 6 GB RAM). The calculation programs for both the DFBEM and the FDTD technique were written in Fortran 90, without using any parallel computing such as multicore processing, clustering, or a graphics processing unit.

Figure 6 is a defect added to the periodic grating shown in Fig. 5(a). The element nodes on C_2 are listed in Table 1. This defect shallows the groove at $-0.25T < x < 0.25T$. The geometry of the defective grating corresponds to Pattern I. The value of n_3 (refractive index in the defect region S_3) was set to 1.5 to represent a defect formed by insufficient etching or ruling. Figure 7(a) is the base field obtained by the method in Ref. [22], while Figure 7(b) is the difference field given by Eqs. (24)–(26). Figure 7(c) is the total field, where the total field within S_3 is equal to that of Fig. 7(b), and the total field within S_1 and S_2 is given by the sum of Fig. 7(a) and Fig. 7(b). The numerical results obtained using the FDTD

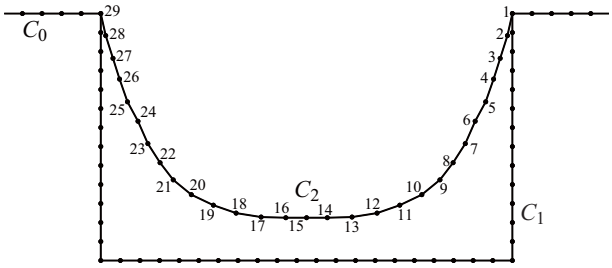

Fig. 6. Profile of the shallow-groove defect. The position for each node is listed in Table 1.

Table 1. Positions of the nodes on the defect surface C_2 numbered in Fig. 6

node	x/T	y/T	node	x/T	y/T
1	0.2500	0.3000	16	-0.02520	0.05200
2	0.2440	0.2732	17	-0.05520	0.05280
3	0.2352	0.2456	18	-0.08560	0.05760
4	0.2272	0.2204	19	-0.1132	0.06720
5	0.2176	0.1928	20	-0.1400	0.08000
6	0.2048	0.1692	21	-0.1620	0.09800
7	0.1928	0.1420	22	-0.1780	0.1188
8	0.1780	0.1188	23	-0.1928	0.1420
9	0.1620	0.09800	24	-0.2048	0.1692
10	0.1400	0.08000	25	-0.2176	0.1928
11	0.1132	0.06720	26	-0.2272	0.2204
12	0.08560	0.05760	27	-0.2352	0.2456
13	0.05520	0.05280	28	-0.2440	0.2732
14	0.02520	0.05200	29	-0.2500	0.3000
15	0.0	0.05200			

method are shown in Fig. 7(d), while the error in the total field between the DFBEM and the FDTD method is also shown in Fig. 7(e). The computational time of the DFBEM was 37.04 s for the base field and 921.0 s (8.416 s for the integral equation solution and 964.0 s for the difference field calculation at $841 \times 266 = 223,706$ points with the integral expression)

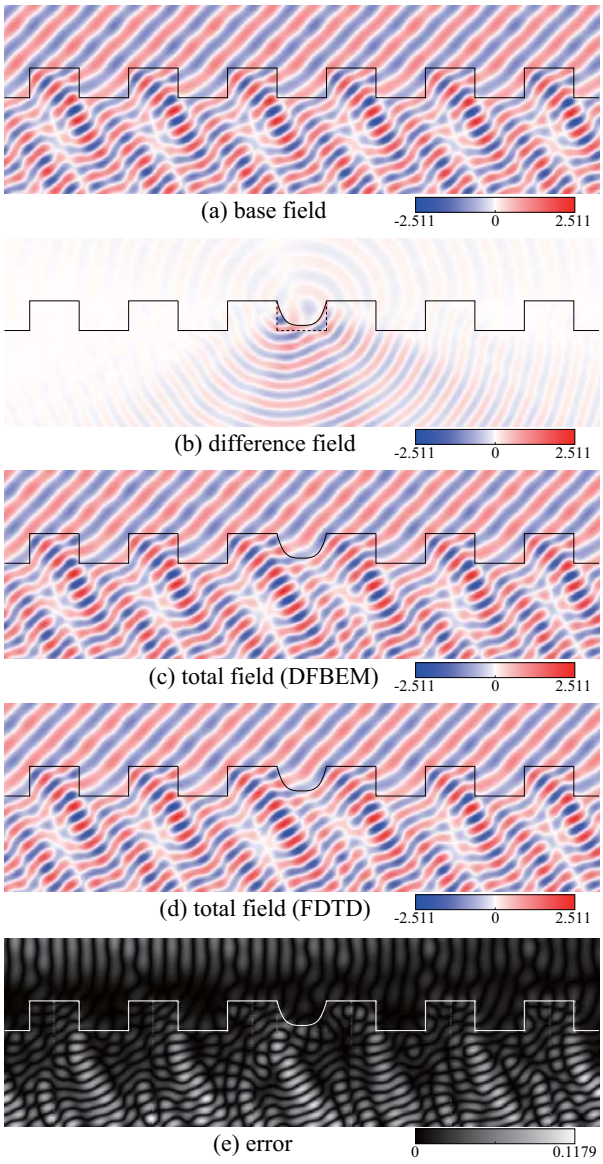

Fig. 7. (a) Base field distribution for the non-defective grating. (b) Difference-field distribution given by Eqs. (24)–(26). (c) Total field distribution obtained from the sum of (b) and (c). (d) Field distribution calculated using the FDTD method. (e) Error in total field between the DFBEM and the FDTD method.

for the difference field calculation, and 37.62 MBytes of memory was consumed. In contrast, the calculation time of the FDTD method was 1,353 s and the memory consumption was 290.6 MBytes.

Figure 8 is a defect added to the periodic grating shown in Fig. 5(b). The element nodes on C_2 are listed in Table 2. The upper-left corner at $x = -0.25T$ is removed by a crack.

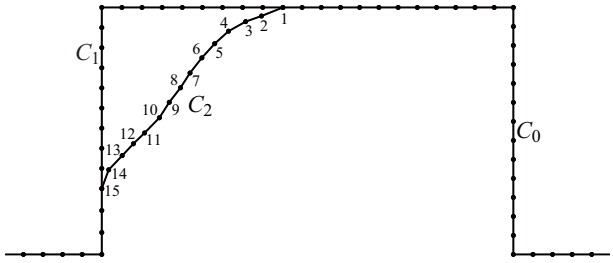

Fig. 8. Profile of the cracked-groove defect. The position for each node is listed in Table 2.

Table 2. Positions of the nodes on the defect surface C_2 numbered in Fig. 8

node	x/T	y/T	node	x/T	y/T
1	-0.03000	0.3000	9	-0.1680	0.1848
2	-0.05600	0.2896	10	-0.1800	0.1660
3	-0.07520	0.2828	11	-0.1980	0.1476
4	-0.09600	0.2712	12	-0.2116	0.1344
5	-0.1128	0.2560	13	-0.2252	0.1200
6	-0.1284	0.2388	14	-0.2416	0.1028
7	-0.1428	0.2204	15	-0.2500	0.08000
8	-0.1544	0.2024			

The geometry of the defective grating corresponds to Pattern II. The value of n_3 was set to 1.0 to represent a cracked corner. The base, difference, and total fields are shown in Figs. 9(a), 9(b), and 9(c), respectively, while the numerical results obtained by the FDTD method are given in Fig. 9(d). The total field error between the DFBEM and the FDTD method (absolute value of the difference) is also shown in Fig. 9(e). The computational time of the DFBEM was 38.20 s for the base field and 900.0 s for the difference field calculations, and the memory consumption was 36.15 MBytes. In contrast, the calculation time of the FDTD method was 1,630 s and the memory consumption was 290.6 MBytes.

Figure 10 is a defect added to the periodic grating shown in Fig. 5(a). The element nodes on C_2 are listed in Table 3. A cylindrical defect parallel to z axis is buried on the bottom of the groove at $x = 0$. The geometry of the defective grating corresponds to Pattern III.

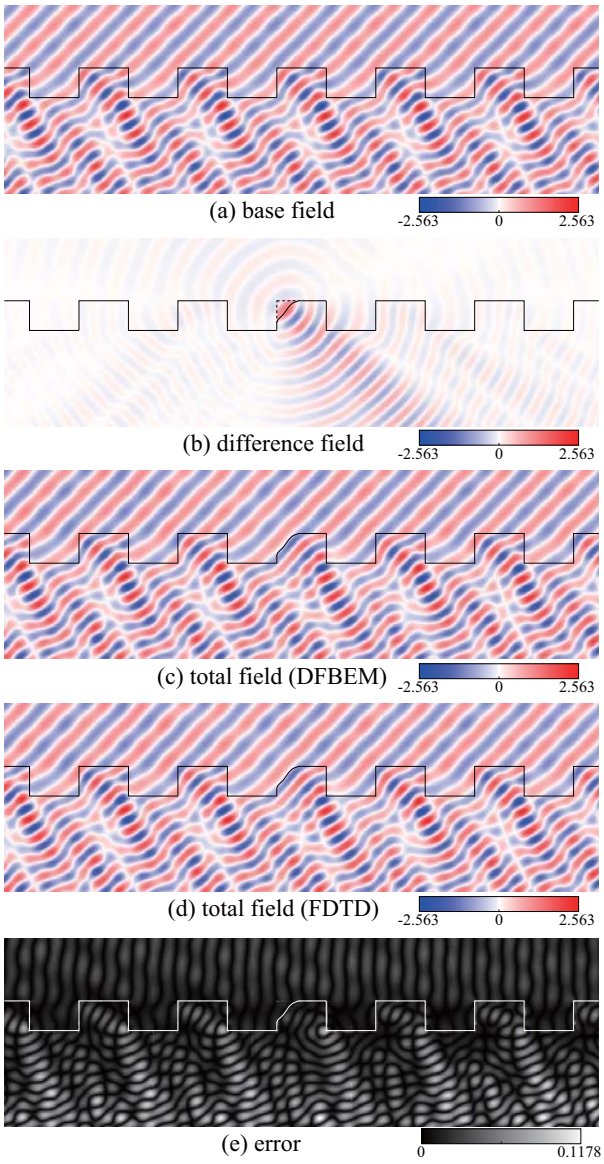

Fig. 9. (a) Base field distribution for the non-defective grating. (b) Difference-field distribution given by Eqs. (41)–(43). (c) Total field distribution obtained from the sum of (b) and (c). (d) Field distribution calculated using the FDTD method. (e) Error in total field between the DFBEM and the FDTD method.

The value of n_3 was set to 1.7 so that S_3 represents a partially buried dielectric. The base, difference, and total fields are shown in Figs. 11(a), 11(b), and 11(c), respectively. The numerical results obtained from the FDTD method are presented in Fig. 11(d), while the total field error between the DFBEM and the FDTD method is also shown in Fig. 11(e). The computational time of the DFBEM was 37.23 s for the base field and 876.5 s for the

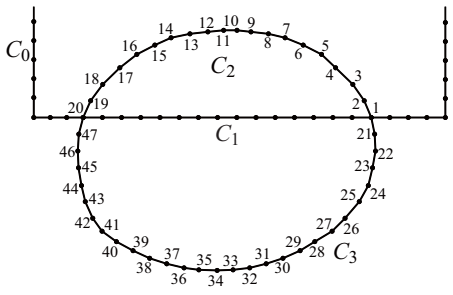

Fig. 10. Profile of the buried-pillar defect. The position for each node is listed in Table 3.

difference field calculations, and the memory consumption was 35.72 MBytes. In contrast, the calculation time of the FDTD method was 1,362 s and the memory consumption was 290.6 MBytes.

Comparing the shape of the wavefront obtained by the DFBEM (Figs. 7(c), 9(c), and 11(c)) to the results from the FDTD method (Figs. 7(d), 9(d), and 11(d)), we find that the results are well matched. The relative errors with respect to each maximum value of the total field are less than 4.695% for Pattern I, 4.596% for Pattern II, and 5.221% for Pattern III. The error distribution in Figs. 7(e), 9(e), and 11(e) is closer to the base field distribution than the difference field distribution. These errors are attributed to the error between the base fields in the BEM and the FDTD method. To estimate the error in the base field, we calculated the base field with the FDTD method and the BEM for the grating (Fig. 5(a)) at $(x, y) = (-0.9571T, -0.6786T)$, where we obtained the maximum error in the total field for Pattern I (Fig. 7(e)). The calculation was performed changing the discretization parameter, $\lambda/\Delta L$. The ΔL corresponds to the Yee-cell size for the FDTD method and the boundary-element length for the BEM. We assumed that the base field for BEM at $\lambda/\Delta L = 30$ is the true value, and plotted the relative error in Fig. 12. Although the convergence speed for the FDTD is slower than that for the BEM, the relative errors are reduced as the $\lambda/\Delta L$ is increased. In the demonstration shown in Figs. 7, 9, and 11, we selected $\lambda/\Delta L = 12$ for the BEM and $\lambda/\Delta L = 40$ for the FDTD method. At these discretization parameters, the relative errors in the base fields for the FDTD method and the BEM are 6.325% and 1.998%, respectively, and the difference, 4.327% is close to the relative error in the total field for Pattern I, 4.596%. Therefore, the error in the total fields of the defective grating is mostly due to the error in the base-field component. More rapid convergence and lower relative error can be achieved by applying such as higher-order boundary elements (linear or

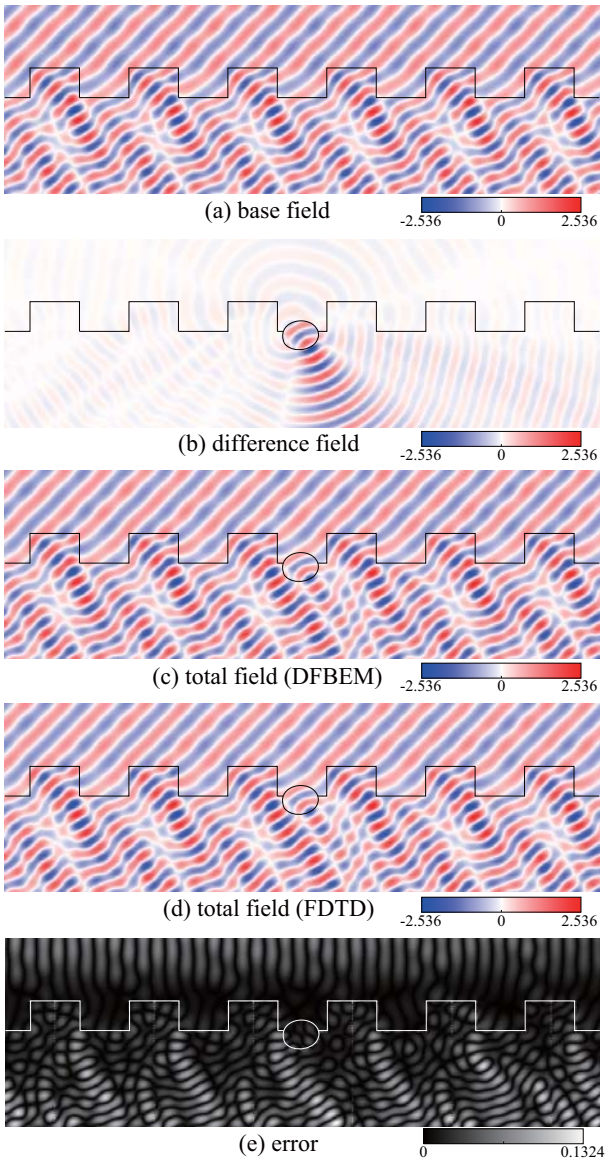

Fig. 11. The refractive index in the defect pillar is 1.7. (a) Base field distribution for the non-defective grating. (b) Difference-field distribution given by Eqs. (58)–(60). (c) Total field distribution obtained from the sum of (b) and (c). (d) Field distribution calculated using the FDTD method. (e) Error in total field between the DFBEM and the FDTD method.

quadratic elements) and higher-order numerical differentiation in the FDTD method. Note that the higher-order boundary elements are applicable to the DFBEM without changing the integral equations and expresssions described in Section 2.

Next, we discuss the convergence of the difference-field component for validating the assumption that the Δf_1 on C_0 decays to zero with increasing distance from the defect. We

Table 3. Positions of the nodes on the defect surface C_2 and C_3 numbered in Fig. 10

node	x/T	y/T	node	x/T	y/T
1	0.1600	0.0	25	0.1455	-0.1022
2	0.1514	0.02037	26	0.1282	-0.1224
3	0.1376	0.04022	27	0.1124	-0.1381
4	0.1167	0.06042	28	0.09137	-0.1508
5	0.09958	0.07667	29	0.07357	-0.1617
6	0.07733	0.08797	30	0.05269	-0.1710
7	0.05526	0.09687	31	0.03232	-0.1777
8	0.03506	0.1017	32	0.01230	-0.1826
9	0.01384	0.1041	33	-0.007907	-0.1850
10	-0.003105	0.1059	34	-0.02725	-0.1857
11	-0.01936	0.1059	35	-0.04950	-0.1850
12	-0.03853	0.1041	36	-0.06747	-0.1826
13	-0.06027	0.10166	37	-0.0885	-0.1777
14	-0.08320	0.09687	38	-0.1092	-0.1710
15	-0.1029	0.08797	39	-0.1294	-0.1617
16	-0.1243	0.07667	40	-0.1496	-0.1508
17	-0.1455	0.06042	41	-0.1671	-0.1381
18	-0.1662	0.04022	42	-0.1784	-0.1224
19	-0.1809	0.02037	43	-0.1874	-0.1022
20	-0.1900	0.0	44	-0.1921	-0.08267
21	0.1641	-0.02020	45	-0.1956	-0.06110
22	0.1651	-0.04073	46	-0.1965	-0.04073
23	0.1615	-0.06110	47	-0.1953	-0.02020
24	0.1564	-0.08267			

calculated the difference fields at the points near the defects; $(x, y) = (0.0, 0.3T)$ for Pattern I, $(x, y) = (-0.35T, 0.2T)$ for Pattern II, and $(x, y) = (0.0, 0.3T)$ for Pattern III, changing

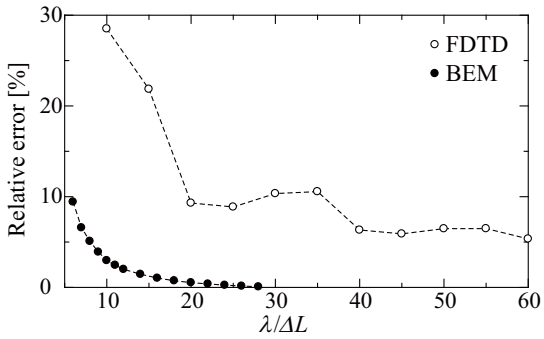

Fig. 12. Convergence of the base field with respect to the discretization parameter ΔL. The parameter ΔL corresponds to the Yee-cell size for the FDTD method and bounary-element length for the BEM. The observation point of the base field is $(x, y) = (-0.9571T, -0.6786T)$ in the periodic grating shown in Fig. 5(a).

the truncated positions $\pm x_t$ of C_0. We considered the difference fields for $x_t = 10.25T$ are the true values, and plotted the relative error in Fig. 13. The difference fields for either three patterns exponentially converged. This results indicate the path integral on C_0 (Eqs. (25), (42), and (59)) at far distance from the defects does not contribute to the difference field at P, and the difference fields on C_0 are also converged to zero at far distance from the defects.

The factor of rapid convergence of the difference field is non-existence of propagation modes on C_0. In addition to that, we discuss another convergence factor, difference fields on C_0 being much less than those on the other boundaries. In the difference field distributions (Figs. 9(b), and 11(b)), the difference field is strongly radiated toward $-45°$. When we regard the difference field with scattering wave from the defects, the strong radiations toward $-45°$ correspond to the forward-scattering. Indeed, in the typical Mie scattering, the forward-scattering becomes largest, and the side-scattering is much less than the forward-scattering and the back-scattering. In the case of the defective grating, the direction along the C_0 is close to the direction of the side-scattering, and thus the difference fields on C_0 are less than those on C_1, C_2, and C_3. Accordingly the integrals on C_0 in the integral expressions for the difference fields, including the effect of C_0 truncation, do not critically contribute the difference fields.

For other defect structures, truncation of C_0 may exhibit the different convergence prop-

erties. The irradiance of the difference field on C_0 (side-scattering) depends on the size and shape of the defect. For example, when the scatterer is much smaller than the wavelength (Rayleigh scattering), the irradiance of the side scattering is comparable to the forward scattering. The incident angle also depends on the convergence property. In the case of shallow incident angle, the forward scattering wave becomes close to the C_0, and the difference field on C_0 would be increased. Hence, when we change the defect structure or incident wave significantly, reexamination of the convergence property is necessary to maintain the accuracy of the calculation result.

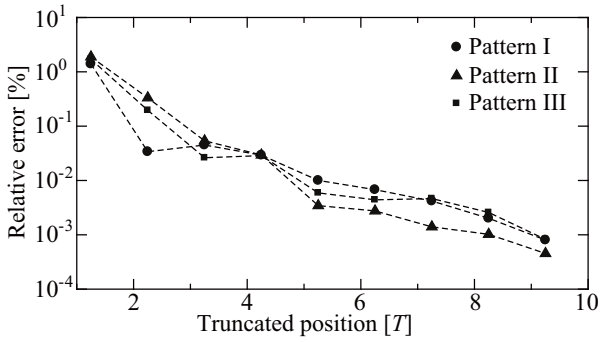

Fig. 13. Convergence of the relative errors in the difference fields at $(x, y) = (0.0, 0.3T)$ for Pattern I, $(x, y) = (-0.35T, 0.2T)$ for Pattern II, and $(x, y) = (0.0, 0.3T)$ for Pattern III, changing the truncated position of the integral paths C_0.

Finally, we validated the boundary conditions of the total field distribution obtained using the DFBEM (Figs. 7(c), 9(c), and 11(c)). For Pattern I, we calculated the field profile across the C_1 and C_2 boundary, as represented by open circles in Figs. 14(a) and 14(b). The lateral axes are given by the n coordinate and the detailed profile positions are shown in Fig. 14(c). The profiles in Figs. 14(a) and 14(b) are calculated along segment AB and segment PQ, respectively. The solid lines in Figs. 14(a) and 14(b) on the S_3 side are drawn so as to pass through the total fields at $n = 0$, with slopes determined by $\partial f_3/\partial n$. Note that $\partial f_3/\partial n$ is included in the solution of the integral equations (14), (15), and (20)–(23). The solid lines on the other side (S_1 or S_2 side) are drawn so as to connect with the solid line for the S_3 side at $n = 0$, with slopes given by $\partial f_3/\partial n$ on the S_3 side and Eq. (5). For example, the slope on the S_1 side is given by $(\varepsilon_1/\varepsilon_3)(\partial f_3/\partial n)$. If the total fields satisfy the theoretical boundary conditions given in Eqs. (4) and (5), the solid lines must be tangent lines of the total fields at $n = 0$, for both the S_3 side and the other side.

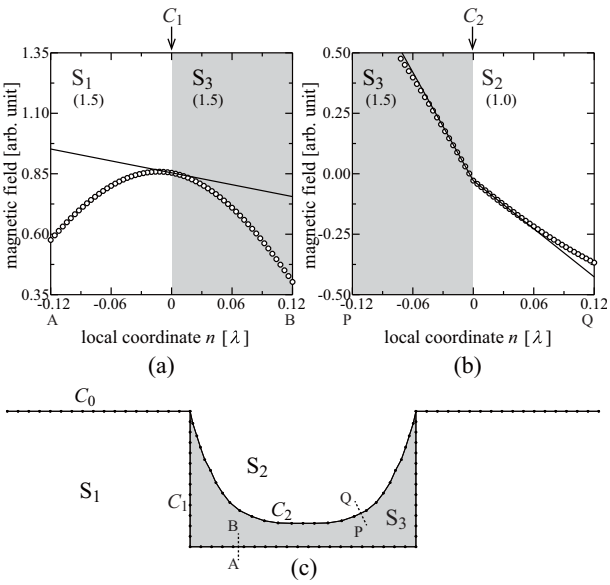

Fig. 14. Total-field profiles across (a) C_1 and (b) C_2. The profile positions are indicated in (c) by the dashed line segments of AB for (a) and PQ for (b). The slopes of the solid lines in (a) and (b) for the S_3 side are given by the integral equations Eqs. (14), (15), and (20)–(23), while that of the other side is determined by the theoretical boundary condition, Eq. (5). Fitting the open circles to the solid lines at $n = 0$ represents the calculated total fields satisfying both the continuity (Eq. (4)) and the theoretical boundary conditions (Eq. (5)).

The total field indicated in Fig. 14(a) continuously and smoothly varies at the boundary C_1, as indicated by the solid line fit to the total-field profile for both the S_3 and S_1 sides. Because the electric permittivities on both sides of C_1 are equal, the total field at C_1 is continuous and differentiable at $n = 0$. Therefore, the total field at C_1 precisely satisfies the boundary condition, even if it is obtained from different equations (sum of f_1 and Δf_1 (Eq. (24)) for the S_1 side or f_3 (Eq. (26)) for the S_3 side, as well as the solution of the integral equation for $n = 0$). As shown in Fig. 14(b), the total-field profile on the dielectric boundary (C_2) must have different slopes on the S_2 and S_3 sides, according to the boundary condition Eq. (5). The calculated total field also fits the polygonal solid line, showing that the total field given by DFBEM satisfies the boundary condition even on the dielectric boundary.

Similarly, we show the total field profiles for Patterns II (Fig. 15) and III (Fig. 16). For Pattern II, Fig. 15(a) is the profile around the boundary (C_1) in the homogeneous medium, and Fig. 15(b) is the profile around the dielectric boundary (C_2). Similar to the

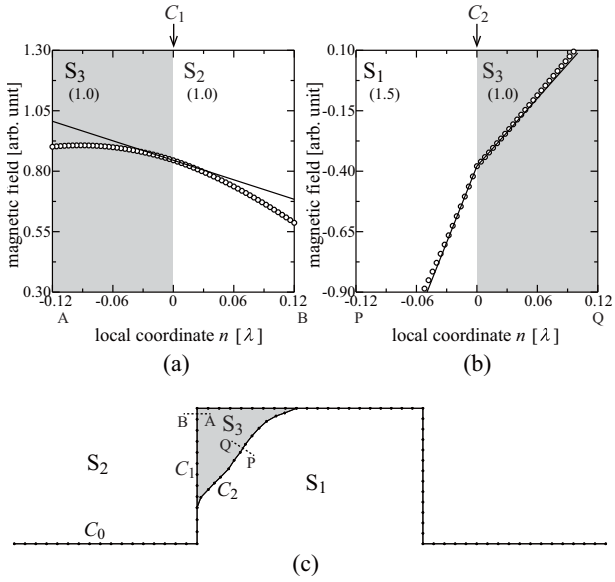

Fig. 15. Total-field profiles across (a) C_1 and (b) C_2. The positions of these profiles are indicated in (c) with the dashed line segments of AB for (a) and PQ for (b). The slopes of the solid lines in (a) and (b) for the S_3 side are given by the integral equations, Eqs. (31), (32), and (37)–(40), while that of the other side is determined from the theoretical boundary condition Eq. (5). Fitting the open circles to the solid lines at $n = 0$ represents the calculated total fields satisfying both the continuity (Eq. (4)) and the theoretical boundary (Eq. (5)) conditions.

profiles for Pattern I, both total field profiles are continuous and fit the solid lines. This result shows that the total field obtained from the integral equations and expressions for Pattern II satisfies the theoretical boundary conditions as well as Pattern I. For Pattern III, Fig. 16(a) is the profile around C_2 (segment AB), and Fig. 16(b) is the profile around C_3 (segment PQ). The total field profiles for both AB and PQ (plotted using open circles) are continuous and fit the solid lines at $n = 0$, indicating the validity of the integral equations and expressions for Pattern III.

4. Conclusion

We have expanded the DFBEM for the analysis of defective gratings with a variety of defect topologies. First, in addition to the original DFBEM, which is capable of computing projection defects, we derived integral equations and expressions for two additional defect types: crack and buried-pillar defects. The integral equations and expressions consist of

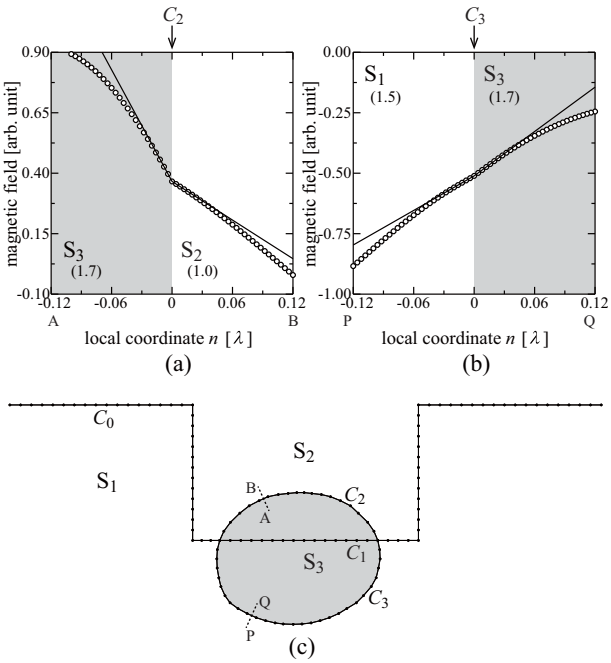

Fig. 16. Total-field profiles across (a) C_1 and (b) C_2. The positions of these profiles are indicated in (c) by the dashed line segments of AB for (a) and PQ for (b). The slopes of the solid lines in (a) and (b) for the S_3 side are given by the integral equation, Eqs. (48), (49), and (54)–(57), while that for the other side is determined by the theoretical boundary condition (Eq. (5)). Fitting the open circles to the solid lines at $n = 0$ represents the calculated total fields satisfying both the continuity (Eq. (4)) and the theoretical boundary (Eq. (5)) conditions.

path integrals on the boundaries around the defect, which is free from infinitely long path integrals. By changing the integral paths, we can analyze different groove types and defect shapes under the conditions that the target structure has a clear dielectric interface, and the topology of the defect is unchanged. As for the material of the grating and the defect, lossless and lossy dielectric, metal and dispersive materials are acceptable, provided the (complex) refractive indices for the wavelength of the illumination light are known. The present DFBEM cannot treat diffraction gratings with propagation modes. Some sort of expression for propagation modes without using the integrals along the diffraction surfaces is necessary. For example, in analyses of the scattering from a waveguide edge, Chien *et al.* have separately treated the scattering-field and propagating-field components [31].

The integral equations and expressions for the two additional defect types have been validated by comparing the field distributions with those obtained using the FDTD method.

The relative error in the field between the DFBEM and the FDTD method is less than 5.221%. Most of the relative error is due to the error in the base-field component. The base-field component with the BEM has a rapid convergence property, whereas that with the FDTD method is slower, and thus we could not sufficiently reduce the relative error. For three defect patterns we described in this paper, we also verified rapid convergence of the difference-field component with DFBEM with respect to the truncated lengths of the integral paths C_0. Considering the rapid convergence for both base-field component with the BEM and the difference-field component with DFBEM, the total fields of the defective gratings also have rapid convergence property for three defect patterns. Although the convergence speed would be changed by such as the angle of the incident wave, size, and shape of the defect, truncation of the C_0 is valid in our derived integral expressions. Finally, we also validated the DFBEM by precisely satisfying the dielectric boundary condition.

In the validation with the FDTD method, we also compared the calculation cost. In our demonstration involving a projection defect (comparable with other types of defects), the DFBEM calculation required 8.416 s at first to solve the integral equation, and then 4.079 ms per point to calculate the difference field. Therefore, when a lesser number of points in the field calculation are required, the DFBEM performs the calculation more rapidly. In contrast, the FDTD method requires many points discretized with Yee's cells, even if the fields at only a few points are required. For example, the simulation of an optical system with a defective grating is an appropriate problem for the DFBEM. Simulations of optical systems can generally be performed only by calculating several far fields radiated from the constituent optical elements. If the number of calculation points is 100, the estimated calculation time for the DFBEM is only $8.416 + 100 \times 4.079 \times 10^{-3} = 8.808$ s, which is 153.7 times less than that of the FDTD method, at 1353 s.

The expanded DFBEM is designed for two-dimensional problems, therefore, the grating is limited to one-dimensional grooves. In the future, we hope to apply the DFBEM to a three-dimensional problem in order to analyze grooves with particle or two-dimensional defects.

References

[1] P. Blattner and H.-P. Herzig, "Rigorous diffraction theory applied to microlenses," J. Mod. Opt. **45**, 1395–1403 (1998).

[2] K. Watanabe, J. Pištora, and Y. Nakatake, "Rigorous coupled-wave analysis of electromagnetic scattering from lamellar grating with defects," Opt. Express. **19,** 25799–25811 (2011).

[3] N. Nguyen-Huu, M. Cada, and J. Pištora, "Imperfectly geometric shapes of nanograting structures as solar absorbers with superior performance for solar cells," Opt. Express. **22,** A282–A294 (2014).

[4] P. Lalanne and E. Silberstein, "Fourier-modal methods applied to waveguide computational problems," Opt. Lett. **25**, 1092–1094 (2000).

[5] E. Silberstein, P. Lalanne, J.-P. Hugonin, and Q. Cao, "Use of grating theories in integrated optics," J. Opt. Soc. Am. A **18**, 2865–2875 (2001).

[6] J. D. Joannopoulos, S. G. Johnson, J. N. Winn, and R. D. Meade, *Photonic crystals: molding the flow of light* (Princeton University Press, 2011).

[7] Y. Xie, A. Zakharian, J. Moloney, and M. Mansuripur, "Transmission of light through slit apertures in metallic films," Opt. Express **12**, 6106–6121 (2004).

[8] A. Vial, A. Erdmann, T. Schmoeller, and C. K. Kalus, "Modification of boundaries conditions in the FDTD algorithm for EUV mask modeling," Proc. SPIE **4754**, 890–899 (2002).

[9] A. Erdmann and C. M. Friedrich, "Rigorous diffraction analysis for future mask technology," Proc. SPIE **4000**, 684–694 (2000).

[10] M. Hakko, T. Kiire, D. Barada, T. Yatagai, and Y. Hayasaki, "Ultraweak background scattered light reveals structure of a diffractive element," Opt. Lett. **38,** 3862–3865 (2013).

[11] K. Dossou, M. A. Byrne, and L. C. Botten, "Finite element computation of grating scattering matrices and application to photonic crystal band calculations," J. Comput. Phys. **219,** 120–143 (2006).

[12] H. Gross, M.-A. Henn, S. Heidenreich, A. Rathsfeld, and M. Bär, "Modeling of line roughness and its impact on the diffraction intensities and the reconstructed critical dimensions in scatterometry," Appl. Opt. **51,** 7384–7394 (2012).

[13] M. Karamehmedovic, M.-P. Sørensen, P.-E. Hansen, and A. V. Lavrinenko, "Application of the method of auxiliary sources to a defect-detection inverse problem of optical diffraction

microscopy," J. Eur. Opt. Soc. Rapid Publ. **5,** 10021 (2010).

[14] J.-M. Jin, S. S. Ni, and S.-W. Lee, "Hybridization of SBR and FEM for scattering by large bodies with cracks and cavities," IEEE Trans. Antennas Propag. **43**, 1130–1139 (1995).

[15] B. Alavikia and O. M. Ramahi, "Finite-element solution of the problem of scattering from cavities in metallic screens using the surface integral equation as a boundary constraint," J. Opt. Soc. Am. A **26**, 1915–1925 (2009).

[16] K. Trotskovsky and Y. Leviatan, "Source-model technique analysis of electromagnetic scattering by surface grooves and slits," J. Opt. Soc. Am. A **28**, 502–510 (2011).

[17] A. Ludwig and Y. Leviatan, "Analysis of arbitrary defects in photonic crystals by use of the source-model technique," J. Opt. Soc. Am. A **21**, 1334–1343 (2004).

[18] J. Sun and C. Zheng, "Numerical scattering analysis of TE plane waves by a metallic diffraction grating with local defects," J. Opt. Soc. Am. A. **26,** 156–162 (2009).

[19] K. Watanabe, J. Pištora, and Y. Nakatake, "Coordinate transformation formulation of electromagnetic scattering from imperfectly periodic surfaces," Opt. Express. **20,** 9978–9990 (2012).

[20] N. Morita, "Surface integral representation for electromagnetic scattering from dielectric cylinders," IEEE Trans. Antennas Propag. **26**, 261–266 (1978).

[21] C. Brebbia, *The Boundary Element Method for Engineers* (Pentech, London, 1978).

[22] Y. Nakata and M. Koshiba, "Boundary-element analysis of plane-wave diffraction from groove-type dielectric and metallic gratings," J. Opt. Soc. Am. A **7**, 1494–1502 (1990).

[23] T. Lu and D. Yevick, "A vectorial boundary element method analysis of integrated optical waveguides," J. Lightwave Technol. **21**, 1793–1807 (2003).

[24] D. W. Prather, M. S. Mirotznik, and J. N. Mait, "Boundary element method for vector modeling diffractive optical elements," Proc. SPIE **2404**, 28–39 (1995).

[25] E. N. Glytsis, M. E. Harrigan, T. K. Gaylord, and K. Hirayama, "Effects of fabrication errors on the performance of cylindrical diffractive lenses: rigorous boundary-element method and scalar approximation," Appl. Opt. **37**, 6591–6602 (1998).

[26] J. Song, N. Zhu, and S. He, "Analysis of the loss resulting from point defects for an etched diffraction grating demultiplexer by using the method of moments," J. Opt. Soc. Am. A, **22,** 1620–1623 (2005).

[27] J. Sugisaka and T. Yatagai, "Fast and highly accurate boundary element method for scattering calculation of defective gratings," Opt. Lett. **37**, 2079–2081 (2012).

[28] V. Rokhlin "Rapid solution of integral equations of classical potential theory," J. Comput. Phys. **60**, 187–207 (1985).

[29] C. C. Lu and W. C. Chew "A multilevel algorithm for solving boundary integral equation," Microwave Opt. Technol. Lett. **7**, 466–470 (1994).

[30] Y. Liu, *Fast multipole boundary element method: theory and applications in engineering* (Cambridge University Press, 2014).

[31] D. N. Chien, M. Tanaka, and K. Tanaka, "Numerical simulation of an arbitrarily ended asymmetrical slab waveguide by guided-mode extracted integral equations," J. Opt. Soc. Am. A. **19,** 1649–1657 (2002).